Computational Medical Physics Working Group Workshop II, Sep 30 – Oct 3, 2007
University of Florida (UF), Gainesville, Florida USA on CD-ROM, American Nuclear Society, LaGrange Park, IL (2007)

An image-based skeletal canine model for pre-clinical evaluations of osteosarcoma molecular radiotherapy

Wesley Bolch[1], Laura Padilla[1], Choonsik Lee[1]
Rowan Milner[2], and Amir Shahlaee[3]
[1]Department of Nuclear & Radiological Engineering
[2]Department of Small Animal Clinical Sciences
[3]Department of Pediatrics
University of Florida
202 NSC, Gainesville, FL 32611
wbolch@ufl.edu; lpr13@ufl.edu; choonsiklee@gmail.com;
MilnerR@mail.vetmed.ufl.edu; shahlah@peds.ufl.edu

ABSTRACT

No canine computational phantoms currently exist as needed for internal organ dosimetry from pre-clinical trials of therapeutic radiopharmaceuticals. In humans, only two broad classes of anatomic phantoms have been developed: stylized (MIRDOSE-3, OLINDA), and voxel phantoms. The voxel based phantoms are anatomically more accurate being derived from image segmentation of either CT or MR images of human anatomy. The objective of this study was to construct a 3D computational phantom of the large dog based on whole-body multi-slice CT data. A female hound-cross underwent whole-body contrast-enhanced CT scanning at 2-mm slice thickness. On completion of the scan, the dog was euthanized and the entire skeleton was harvested for subsequent microCT investigation. The CT data was imported into the computational software 3D-Doctor® and used to create a polygon mesh phantom of the entire animal. All the major organs and bones were semi-automatically segmented and tagged to the CT slices. The phantom was then imported into the Rhinoceros® software and transformed into a Nonuniform Rational B-Splines (NURBS) surfaces phantom, allowing easy alteration of the phantom to simulate dogs of smaller or larger stature. The canine phantom was then re-voxelized using an in-house MATLAB® routine and is thus ready for radiation transport calculations of photon and beta-particle organ dosimetry. Completion of this phantom will help us to assess photon dose throughout the various radiosensitive organs of the dog phantom during targeted radiopharmaceutical therapy trials. The model will later be complemented by a detailed microstructural model of trabecular spongiosa and bone marrow tissues.

KEYWORDS: canine phantom, NURBS models, radiation dosimetry, photon cross-dose, preclinical animal models.

1. INTRODUCTION

With the recent completion of the canine genome project [1,2] and the recognition of the similarities between canine cancers and human cancers [3], it is now clear that dogs are an effective model for preclinical development of novel antineoplastic agents [4]. Rodents and larger animals such as non-human primates have been used in cancer research for many years. Although the availability and short lifespan of mice and rats make them a useful investigative tool for new drugs, the results obtained from these studies must be extrapolated to humans with possibly large uncertainties. In radiopharmaceutical research, the much smaller anatomical dimensions in the rodent in comparison to human subjects can result in vastly different patterns of energy deposition among tissues of interest [5]. As a result, dosimetry estimates and dose-response relationships are complicated and not easily extrapolated to humans [6]. On the other hand, research performed with non-human primates can be more fruitful, but it is hardly the best option due to the limited availability and cost of these animals. Accordingly, cancer research using canine subjects is ideal as there is a the large population available [approximately 4 million dogs are diagnosed with cancer each year in the U.S. [3]] and many histological and biochemical similarities exist between canine and human diseases [7,8].

Nevertheless, before radiopharmaceutical canine studies can reach their full potential, computational and dosimetry tools must be available for researchers to fully utilize canine models of human disease. At present, no canine dosimetry model exists to evaluate the radiation doses during preclinical studies. Veterinary doctors and researchers accordingly have had to rely on human dosimetry software such as MIRDOSE v3.1 [9] and OLINDA/EXM v1.0 [10] to perform their calculations [11-14]. While current efforts are underway to update the OLINDA code to include voxel-based anatomic phantom dosimetry [15], present versions of both these codes utilized human stylized phantoms from the Oak Ridge National Laboratory (ORNL) series [16].

2. MATERIALS AND METHODS

This study was approved by the University of Florida Institutional Animal Care and Use Committee and was performed in accordance with the Institute for Lab Animal Research Guide for the Care and Use of Laboratory Animals. A 24 kg, 3-year-old female hound-cross dog was selected based upon her size and bred, but deemed to be representative of a broad range of canine subjects, and thus offering the external and internal anatomy necessary to establish an initial reference canine phantom. Prior to enrollment, the dog was certified to be disease-free and not on any medications. Furthermore, this dog represents a phenotype that is commonly used as a model for human disease including various forms of bone cancer [4].

Anesthesia was induced intravenously using propofol infusion (120 mg) and maintained using 1-2% isoflurane. The dog was scanned in a prone position using a Philips Tomoscan-M multi-slice CT scanner. The X-ray tube was set at 120 kVp and 10 mA. The field of view was 35 cm x 35 cm and image reconstruction was performed a grid of 512 x 512 pixels. The slice thickness was set at 2 mm. The scan was performed in 3 overlapping sections: (1) head and neck, (2) thorax

and abdomen, and (3) pelvis and tail. At the start of the study, the dog was given 200 mL Iohexol (300mg/ml) for contrast enhancement and this was repeated with each scan section. On completion of the CT study, the dog was euthanized (20 ml Beuthanasia-D Special, Schering-Plough Animal Health Corp, USA) and the complete skeleton was harvested. The individual bones were cleaned using atraumatic technique (beetle box) and preserved for later ex-vivo CT and in-vitro microCT studies of the skeletal architecture at both a macroscopic and microscopic level.

A total of 29 tissues and 19 skeletal sites were selected for model construction of the canine anatomic phantom. As shown in Table 1, these organs were based primarily on those listed in ICRP Publication 89 [17] for human radiological protection dosimetry. All non-segmented regions of the body such as adipose tissue, skeletal muscle, major bloods vessels, lymphatic tissues, and connective tissues were denoted as *residual soft tissues* (RST) and assigned as a single tissue region.

Following CT scanning, the resultant images were imported to *3D-Doctor*^{TM} (Able Software Corp., Lexington, MA), a 3D modeling and image processing software for tomography data, where organs of interest were segmented semi-automatically within each axial CT image. Tissue regions were tagged with organ identifiers for later use in radiation transport modeling and 3D image visualization. The individual organ contours were subsequently joined in the assembly of a polygon-mesh model of each individual organ, as well as the outer body contour of the animal.

Some smaller organs within the CT image were difficult to visualize owing to low image contrast. These include the pituitary gland, thymus, adrenal glands, and ovaries. These organs were inserted manually within the phantom based on an anatomical text reference [18] and by concurrence with our veterinary oncologist (R Milner).

Following its construction within 3*D-Doctor*^{TM}, organ-specific polygon-mesh models were imported to a second software program, *Rhinoceros*^{TM} used to fit NURBS surfaces to each polygon representation of the phantom's tissues and organs. To manipulate polygon anatomic models independently and effectively, *Wavefront Object* files were generated from *3D-Doctor*^{TM} in 5 different groups: (1) the exterior body contour, (2) the alimentary system, (3) the respiratory system, (4) other soft-tissue organs, and (5) the skeleton. Each group of organs were then imported as different layers within *Rhinoceros*^{TM}. In this manner, each layer could be turned on or off with objects within other layers being unaffected. Smooth NURBS surfaces were created from these polygon mesh models on an organ-by-organ basis. First, several contours were obtained from the polygon mesh model as needed, and NURBS surfaces were fit to these contours using tools within the software. NURBS surfaces were generated for all internal organs and tissues. The single exception, however, was the skeleton whose complex 3D structure was best persevered within the polygon-mesh model of 3*D-Doctor*^{TM}.

The small intestine and colon were difficult to visualize within the CT images, again owing to low image contrast, as well as their complex anatomic geometry. Consequently, these organ structures were created as follows. First, the outer boundaries of the canine gut were traced within the CT images using *3D-Doctor*^{TM}. Next, the CT images were used to define a central trace of the colon lumen, after which a NURBS pipe model was constructed to define the colon

wall. A similar approach was employed for the small intestine with the small intestinal length and wall thickness matched to values indicated as "representative" based on canine anatomical references [18].

Several walled organs were also modeled directly within *Rhinoceros*™. These included the esophagus, heart, stomach, gall bladder, and urinary bladder. Visualization of the esophagus was possible in only some of the axial CT slices and thus, as with the gut model, a NURBS pipe structure was employed that gave a representative thickness and length of the esophagus that was both consistent with the CT images and anatomical references [18].

In the format of their polygon-mesh model, the ribs appeared stair-stepped due to the limited slice-thickness of the organ CT image set and their 3D orientation relative to the slice plane. Consequently, the entire ribs cage was remodeled using NURBS surfaces. Costal cartilage that was not fully represented in the polygon-mesh model was manually included in the NURBS version of the skeletal site. Following model completion, it was seen that the urinary bladder of the subject was overly full due to the injection of contrast agent at the time of CT imaging. The urinary bladder was thus modified in *Rhinoceros™* to reduce the organ to a more standard size. A side-by-side comparison of the polygon-mesh version and the NURBS surface version of the UF canine phantom are shown in Figures 1B and 1C, respectively, with a surface rendering of the original CT image set shown in Figure 1A.

Internal dosimetry calculations were performed using the EGSnrc radiation transport code [19] which required a voxelized version of the canine phantom. To prepare the phantom for voxelization, the finalized NURBS-based phantom was exported as a group of polygon-mesh objects with each organ assigned a relative level of importance required to resolve organ overlap issues during the voxelization process. Model voxelization was accomplished via an in-house MATLAB™ code *Voxelizer [20]*. The resulting voxel version of the UF canine phantom is shown in Figure 1D. The final voxel resolution of the phantom was set at 2 x 2 x 2 mm^3 based primarily on the need to properly represent the epidermis/dermis of the animal as a single voxel layer in the final model.

Four tissue media were used for the radiation transport calculations: air, soft tissue, skeleton (homogeneous mixture of bone and marrow), and lung (homogeneous mixture of soft tissue and air). As no comprehensive reference values exist for tissues and organs within the adult dog, the elemental composition and mass densities of these materials were taken as those used in ORNL/TM-8381 for the stylized ORNL human phantom series [16]. Photon and electron source energies from 10 keV to 4 MeV were also chosen radiation transport simulation at an energy grid equivalent to that used in ORNL/TM-8381. Particle histories were set at 10^8 per source organ at energies below 100 keV and 10^7 particles at energies above 100 keV.

The skeletal tissues in the present canine phantom are homogeneous and thus we cannot at present report values of cortical bone, trabecular bone, and red and yellow bone marrow throughout this subject. A more detailed skeletal model (including the trabecular and marrow cavity microstructure) for this phantom is currently in progress. Consequently, the absorbed dose to homogeneous skeleton was tabulated for both internal photon and electron sources. As new data on the skeletal microstructure and corresponding electron dosimetry become available,

it will the be possible to replace values of homogeneous skeletal absorbed dose with values explicitly detailing energy deposition to the canine active bone marrow and skeletal endosteum.

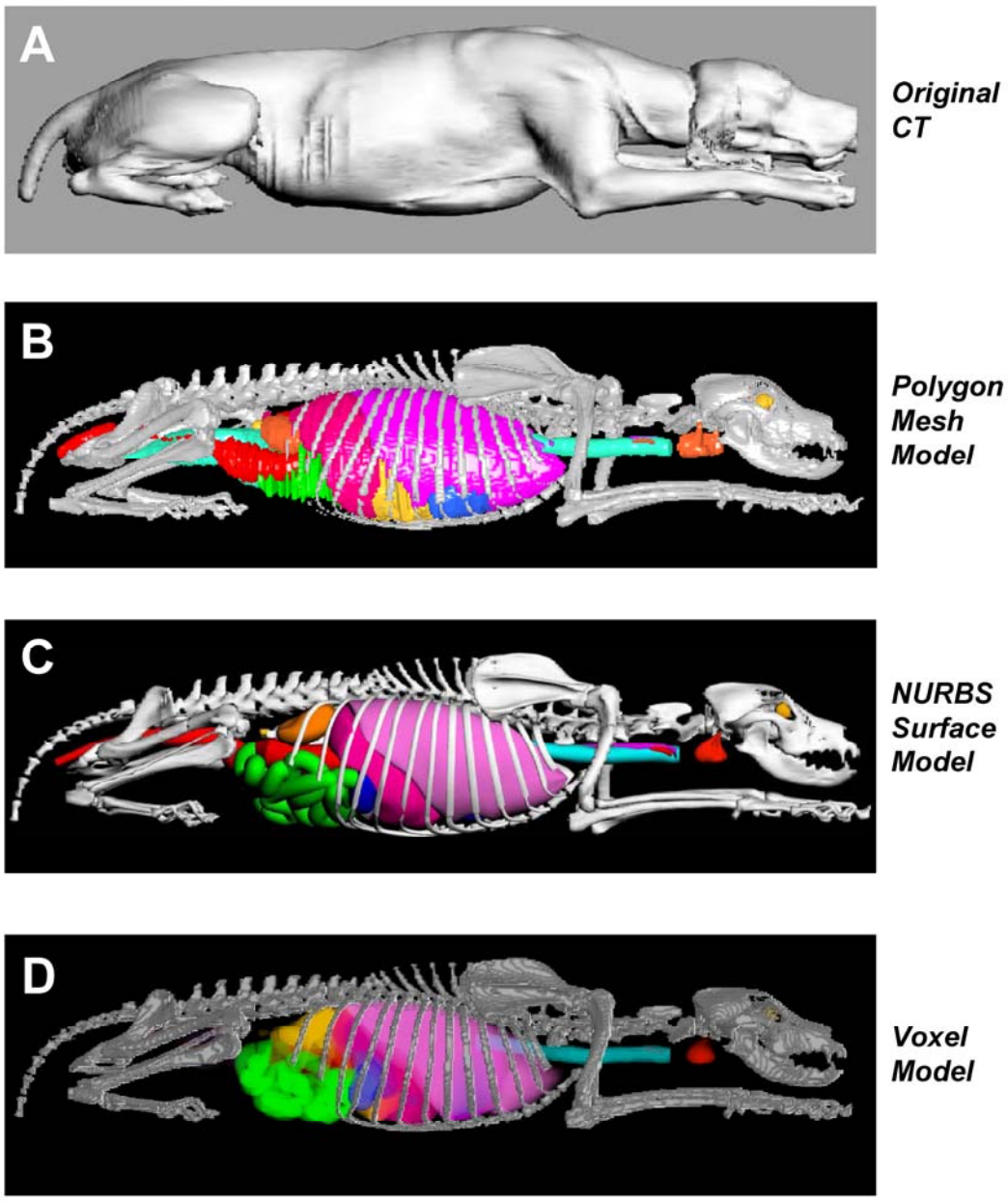

Figure 1. Visual comparison of different versions of the UF hybrid canine phantom: (A) surface rendering of the original CT image set, (B) polygon-mesh model of *3D-Doctor*™, (C) NURBS surface model of *Rhinoceros*™, and (D) voxel-based model from the MATLAB™ code *Voxelizer*.

3. RESULTS

In Table 1, we list the final organ volumes and organ masses as they appear in the voxel-version of the UF canine phantom (Figure 1D). Tissues are listed by organ system, and the standardized ORNL/TM-8381 tissue densities assumed are noted as well. Residual soft tissues (e.g., tissues and organs not segmented) are given within the *Additional Tissues* category and include separable fat, muscle, major blood vessels, lymphatic nodes, and connective tissue. The recorded total body mass of the animal as 24 kg at the time of CT scanning. The total body mass of the voxel version of the canine phantom as 26.0 kg, and with the removal of all interior fluids of walled organs, the total body tissue mass of the animal model came to 24.5 kg.

Table 1. Segmented organs and their volumes and masses within the hybrid-voxel UF canine phantom.

Organ System	Density (g/cm^3)	Organ Volume (cm^3)	Organ Mass (g)
Respiratory System			
Trachea - wall	1.04	37.51	39.01
Lung (Left)	0.296	630.81	186.72
Lung (Right)	0.296	1119.54	331.38
Totals:		*1787.86*	*557.11*
Alimentary System			
Salivary glands	1.04	30.36	31.57
Esophagus - wall	1.04	11.11	11.56
Stomach - wall	1.04	66.02	68.66
Stomach - contents	1.04	316.24	328.89
Small Intestine - wall	1.04	176.78	183.85
Small Intestine - contents	1.04	494.64	514.43
Colon - wall	1.04	180.26	187.47
Colon - contents	1.04	296.79	308.66
Liver	1.04	680.58	707.80
Gall Bladder - wall	1.04	1.01	1.05
Gall Bladder - contents	1.04	5.98	6.22
Pancreas	1.04	1.83	1.91
Totals:		*2261.61*	*2352.07*
Circulatory System			
Heart - wall	1.04	170.97	177.81
Heart - content	1.04	236.85	246.32
Totals:		*407.82*	*424.13*
Urogenital System			
Kidney (Left)	1.04	98.05	101.97
Kidney (Right)	1.04	96.92	100.80
Urinary Bladder - wall	1.04	30.09	31.29
Urinary Bladder - contents	1.04	97.54	101.44
Ovary (Left)	1.04	1.384	1.44
Ovary (Right)	1.04	0.59	0.62
Uterus	1.04	3.976	4.14
Totals:		*328.54*	*341.69*
Integumentary System			
Skin	1.04	2000.04	2080.04

Organ System	Density (g/cm^3)	Organ Volume (cm^3)	Organ Mass (g)
Skeletal System			
Cranium	1.40	174.20	243.88
Mandible	1.40	82.11	114.96
Scapulae	1.40	99.50	139.29
Sternum	1.40	12.90	18.07
Ribs	1.40	113.77	159.28
Coastal cartilage	1.40	37.95	53.13
Vertebrae (cervical)	1.40	118.80	166.32
Vertebrae (thoracic)	1.40	129.84	181.78
Vertebrae (lumbar)	1.40	129.15	180.81
Sacrum	1.40	24.69	34.56
Vertebrae (caudal)	1.40	26.82	37.55
Os Coxae	1.40	105.19	147.27
Femur - upper half	1.40	80.56	112.78
Femur - lower half	1.40	82.40	115.36
Tibiae	1.40	112.44	157.42
Fibulae	1.40	8.46	11.85
Hind paw bones	1.40	53.29	74.60
Humerus - upper half	1.40	72.22	101.11
Humerus - lower half	1.40	73.02	102.22
Radii	1.40	62.81	87.93
Ulnae	1.40	53.66	75.13
Front paw bones	1.40	97.79	136.91
Totals:		*1751.58*	*2452.22*
Additional Tissues			
Air passages	0.0012	64.78	0.08
Adrenal Gland (Left)	1.04	0.18	0.19
Adrenal Gland (Right)	1.04	0.11	0.12
Brain	1.04	82.83	86.15
Eyes	1.04	9.36	9.73
Pituitary gland	1.04	0.016	0.02
Spinal cord	1.04	18.104	18.83
Spleen	1.04	362.37	376.86
Thymus	1.04	0.76	0.79
Thyroid	1.04	0.94	0.98
Residual Soft Tissues (RST)	1.04	16679.90	17347.09
Totals:		*17219.35*	*17840.84*

Total Body Tissues (kg)	24.5
Total Body Mass (kg)	26.0

Prior to the establishment of the current phantom, the 10-year-old stylized human phantom of the MIRDOSE program has been used as an approximate model for assessing internal organ doses in preclinical canine studies of both diagnostic and therapeutic radiopharmaceuticals. The selection of this particular human-like phantom was based on consideration of not only total body mass, but also individual organ sizes and torso length. The total body mass of the ORNL 10-year human phantom is 33.2 kg (1.3 times heavier than the UF canine phantom), while the total body mass of the ORNL 5-year human phantom is 19.8 kg (80% of the mass of the UF canine phantom). To further explore the appropriateness of the 5-year versus 10-year ORNL phantoms

as surrogate canine phantoms, we show individual organ masses for all three phantoms in Figure 2. Five of the organs within the UF canine phantom are significantly smaller than either ORNL human phantom: adrenal glands, brain, gall bladder wall, pancreas, and thyroid. The colon wall and skin are noted to be appreciably more massive than their ORNL organ models. Total body mass, as well as rest-of-body mass, of the UF canine phantom are intermediate to the two ORNL human phantoms, while the total skeleton mass in more closely approximated by the 5-year human phantom.

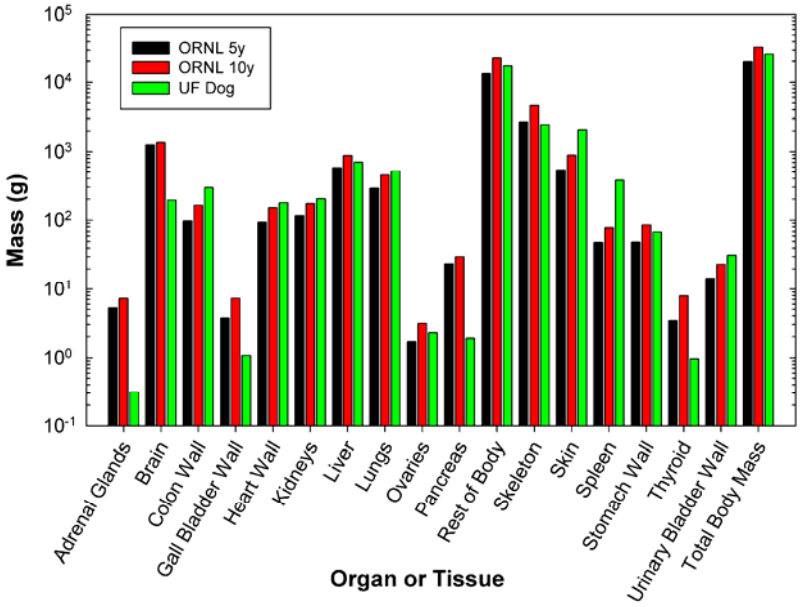

Figure 2. Graphical comparison of individual organ masses in the UF canine phantom, the ORNL 5-year human phantom, and the ORNL 10-year human phantom.

4. DISCUSSION

Of importance to photon cross-fire are not only the mass of the source and target organs, but their 3D shapes, locations, and positions which can vary considerably between image-based anatomic models such as the UF canine phantom, and the stylized anatomic models such as the ORNL human phantoms. In Figures 3A to 3D, we compare selected values of specific absorbed fractions to various target tissues for photon sources localized in the skeleton, liver, spleen, and kidneys, respectively, within each of the three phantoms – UF canine, ORNL 5-year-old, and ORNL 10-year-old. While the total body mass of the UF canine phantom is intermediate to that of the ORNL 5-year and 10-year phantoms, the skeletal mass is very close to that in the ORNL 5-year phantom. Values of Φ(lungs ← skeleton) are shown to be intermediate to values given by the two human stylized phantoms, while values of Φ(small intestine wall ← skeleton) of Figure 3A are shown to considerably lower in the UF canine phantom. Data of Figure 3B for photon sources in the liver indicate substantially higher values of absorbed dose per photon emission to the lungs and stomach wall of the UF canine phantom than indicated from transport simulations in the ORNL phantoms.

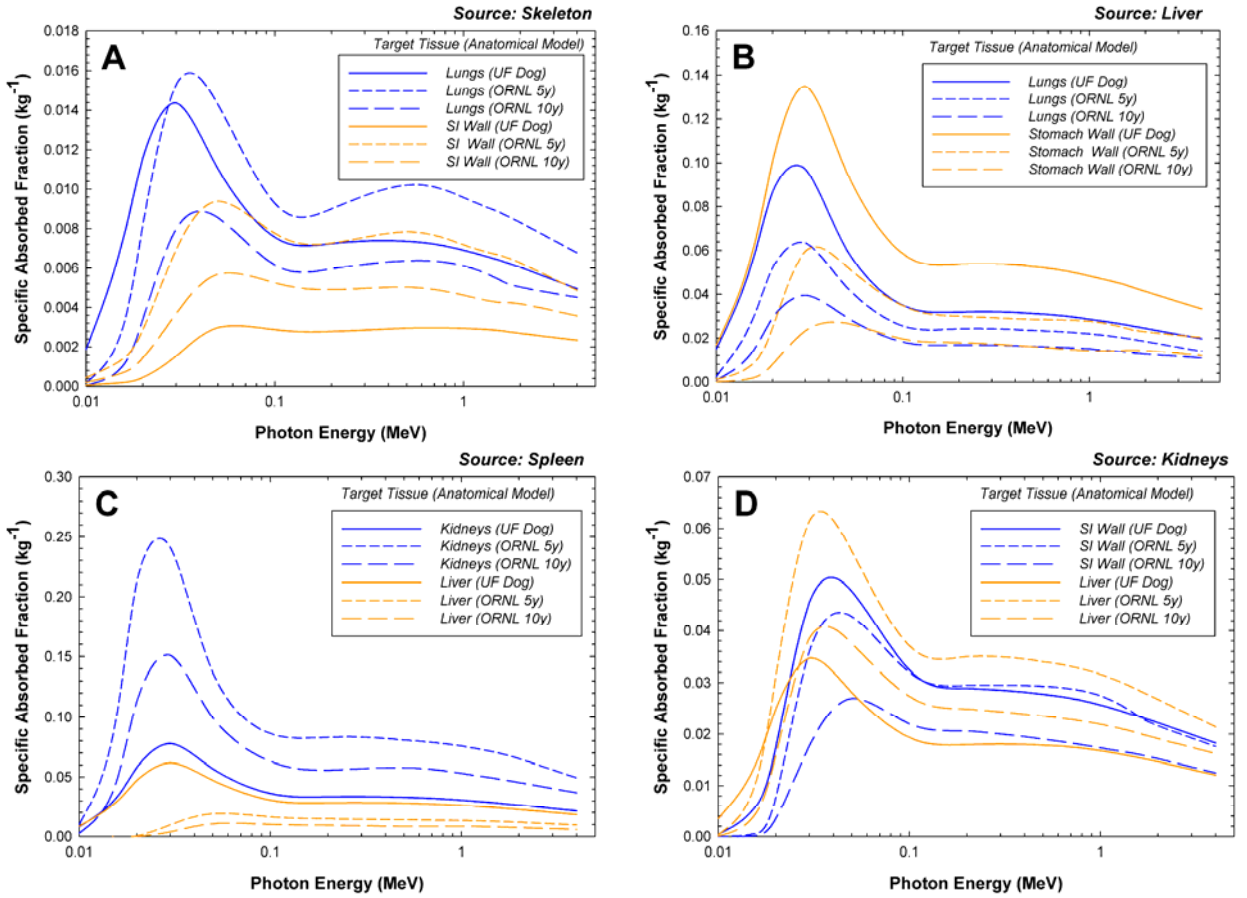

Figure 3. Specific absorbed fractions to various target tissues in the UF canine, ORNL 5-year, and ORNL 10-year phantoms for photon sources in (A) the skeleton, (B) liver, (C) spleen, and (D) kidneys.

For photon sources in the spleen (Figure 3C), cross-dose to the kidneys within the UF canine phantom is shown to be much lower than seen in either the ORNL 5-year or 10-year phantoms. In contrast, both ORNL phantoms demonstrate much lower values of Φ(liver ← spleen) across all photon energies than indicated by the internal organ anatomy of the UF canine phantom. In Figure 3D, photon sources are localized in both kidneys, and organ cross-dose to the small intestine wall and liver are explored as a function of photon energy and phantom anatomy. For values of Φ(small intestine wall ← kidneys), higher values are seen in the UF canine phantom at energies below 100 keV, above which their values are best approximated by the smaller 5-year ORNL phantom. Cross-organ irradiation of the liver by photon sources in the spleen are shown to be substantially lower in the UF canine phantom than in either ORNL phantom.

Differences in photon cross-fire may be attributed to a number of parameters such as the masses of the source and target organs, as well as their shapes, positions, and orientation with respective to one another in a given anatomic phantom. For example, consider the large discrepancies in Φ(lungs ← liver) and Φ(stomach ← liver) between the ORNL phantoms and the UF canine phantom as displayed in Figure 3B. Mass differences between the liver and lungs in the 10-year ORNL phantom are very similar to those in the UF canine phantom (see Fig. 2), and thus differences in photon cross-fire dose must be attributed to issues of 3D spatial orientation

between organ pairs. Side-by-side views of the torso internal organ anatomy of the ORNL 10-year stylized human phantom (left) and UF NURBS-based canine phantom (right) are shown in both anterior and posterior views within Figures 4A and 4B, respectively. In these figures, we see that a large portion of the superior surface of the liver in the canine phantom is in direct contact with the inferior surfaces of the left and right lungs (Figs. 4B and 4D). Similarly, a sizable portion of the inferior surface of the canine liver is in direct contact with the later reaches of the canine stomach (Fig. 4B). In contrast, Figures 4A and 4C demonstrate that virtually no direct organ-to-organ contact is maintained in the more fixed and rigid organ modeling of the ORNL human 10-year phantom. Consequently, photons at all energies have more tissue attenuation and scatter in the stylized phantom, in comparison to that of the more realistic dog anatomy.

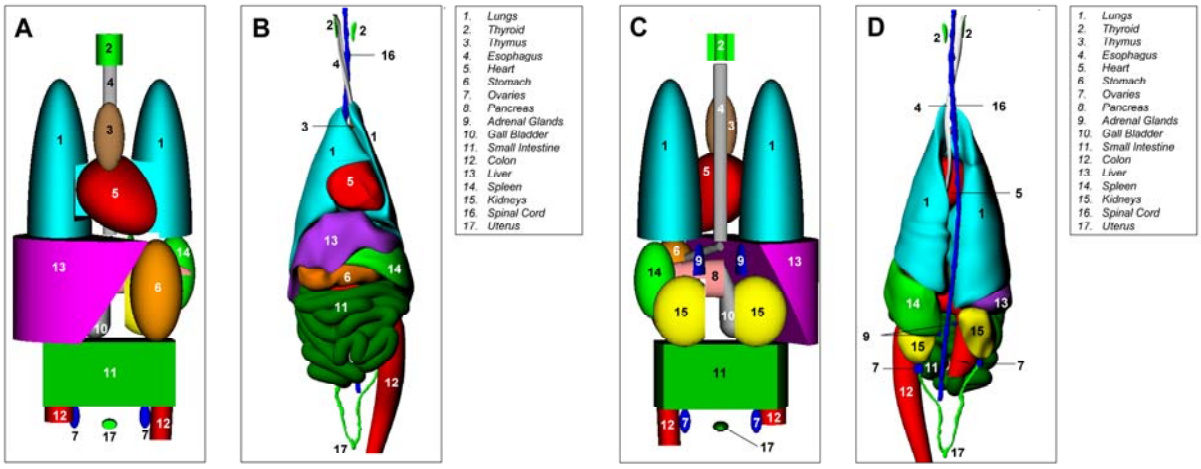

Figure 4. Anatomical comparisons between the UF canine model and the ORNL 10-year stylized phantom in (A) the anterior view, and (B) the posterior view.

3. CONCLUSIONS

The use of canine models, particularly in spontaneously occurring malignancies such as osteosarcoma, for preclinical testing of antineoplastic agents offers significant advantages over current murine models. However, development of canine-specific technology is critical to the optimization of these studies. The UF canine dosimetry phantom presented in this article aims to solve possible problems that could stem from using current human-based dosimetry models during radiopharmaceutical research. As discussed previously, human-based models, such as the stylized ORNL phantoms used in MIRDOSE and OLINDA software, can lead to potentially significant errors in the assessment of photon cross-fire within the canine animal model. For example, values of specific absorbed fraction to the lungs from 30 keV photons emitted with the liver are shown in the ORNL 5-year and ORNL 10-year phantoms to underestimate their corresponding value in the UF canine phantom by factors of 3 to 4.5. Future studies will further define the masses and skeletal site distribution of cortical bone, trabecular bone, and red and yellow bone marrow in this animal. Finally, the techniques employed – namely NURBS surface modeling – can be extended to the both the construction of other dog breeds and animal sizes, and can be used to alter body shape and rest-of-body mass to more explicitly model individual animals in a pre-clinical dosimetry study. These same techniques are currently being used to also expand the availability of human phantoms for internal dose assessment [15,21].

REFERENCES

1. Lindblad-Toh K, Wade CM, Mikkelsen TS, *et al.* Genome sequence, comparative analysis and haplotype structure of the domestic dog. *Nature.* 2005;438:803-819.
2. Starkey MP, Scase TJ, Mellersh CS, Murphy S. Dogs really are man's best friend--canine genomics has applications in veterinary and human medicine! *Brief Funct Genomic Proteomic.* 2005;4:112-128.
3. Vail DM, MacEwen EG. Spontaneously occurring tumors of companion animals as models for human cancer. *Cancer Invest.* 2000;18:781-792.
4. Khanna C, Lindblad-Toh K, Vail D, *et al.* The dog as a cancer model. *Nat Biotechnol.* 2006;24:1065-1066.
5. Stabin MG, Peterson TE, Holburn GE, Emmons MA. Voxel-based mouse and rat models for internal dose calculations. *J Nucl Med.* 2006;47:655-659.
6. NCRP. *Extrapolation of radiation-induced cancer risks from nonhuman experimental systems.* Report No. 150. Bethesda, MD: National Council on Radiation Protection and Mesurements; 2005.
7. Sargan DR. IDID: inherited diseases in dogs: web-based information for canine inherited disease genetics. *Mamm Genome.* 2004;15:503-506.
8. Patterson D. Companion animal medicine in the age of medical genetics. *J Vet Inten Med.* 2000;14:1-9.
9. Stabin MG. MIRDOSE: personal computer software for internal dose assessment in nuclear medicine. *J Nucl Med.* 1996;37:538-546.
10. Stabin MG, Sparks RB, Crowe E. OLINDA/EXM: the second-generation personal computer software for internal dose assessment in nuclear medicine. *J Nucl Med.* 2005;46:1023-1027.
11. Desrosiers MF, Avila MJ, Schauer DA, Coursey BM, Parks NJ. Experimental validation of radiopharmaceutical absorbed dose to mineralized bone tissue. *Appl Radiat Isot.* 1993;44:459-463.
12. Milner RJ, Dormehl IC, Louw WKA, Chaparro F, Kilian E. The biodistribution, pharmacokinetics, bone localization, and therapeutic effect of Rhenium-188-HEDP in normal dogs and dogs with osteosarcoma of the appendicular skeleton [Abstract]. *Eur J Nucl Med.* 1998;25:1109.
13. Louw WKA, Dormehl IC, Milner RJ, *et al.* Biodistribution of radiolabeled ploymin-MP of different molecular sizes as a selective bone seeker for therapy in animal models [Abstract]. *Eur J Nucl Med.* 1998;25:1167.
14. Milner RJ, Dormehl IC, Louw WKA, Kilian E. The biodistribution, pharmacokinetics, and bone localization of variously sized molecular radiolabeled polymin-MP in normal dogs and dogs with osteosarcoma of the appendicular skeleton [Abstract]. *Eur J Nucl Med.* 1999;26:1120.
15. Stabin M. Nuclear medicine dosimetry. *Phys Med Biol.* 2006;51:R187-202.
16. Cristy M, Eckerman KF. *Specific absorbed fractions of energy at various ages from internal photon sources.* ORNL/TM-8381/Volumes I-VII. Oak Ridge, TN: Oak Ridge National Laboratory; 1987.

17. ICRP. *Basic anatomical and physiological data for use in radiological protection: reference values.* Publication 89. Oxford; Pergamon Press: International Commission on Radiological Protection; 2002.
18. Miller ME. *Anatomy of the Dog.* Philadelphia, PA: WB Saunders Company;1993.
19. Kawrakow I. Accurate condensed history Monte Carlo simulation of electron transport. I. EGSnrc, the new EGS4 version. *Med Phys.* 2000;27:485-498.
20. Lee C, Lodwick D, Hasenauer D, Williams JL, Lee C, Bolch WE. Hybrid computational phantoms of the male and female newborn patient: whole-body models. *Phys Med Biol.* 2007;52:3309-3333.
21. Lee C, Lee C, Lodwick D, Bolch WE. NURBS-based 3D anthropometric computational phantoms for radiation dosimetry applications. *Radiat Prot Dosim.* 2007;(doi:10.1093/rpd/cm277):